MIT Open Access Articles

Ultra-Short Nacelles for Low Fan Pressure Ratio Propulsors

Citation: Peters, Andreas, Zoltán S. Spakovszky, Wesley K. Lord, and Becky Rose. "Ultra-Short Nacelles for Low Fan Pressure Ratio Propulsors." Volume 1A: Aircraft Engine; Fans and Blowers (June 16, 2014).

As Published: http://dx.doi.org/10.1115/GT2014-26369

Publisher: American Society of Mechanical Engineers

Persistent URL: http://hdl.handle.net/1721.1/116091

Version: Final published version: final published article, as it appeared in a journal, conference proceedings, or other formally published context

Massachusetts Institute of Technology

ULTRA-SHORT NACELLES FOR LOW FAN PRESSURE RATIO PROPULSORS

Andreas Peters and Zoltán S. Spakovszky
Gas Turbine Laboratory
Massachusetts Institute of Technology
Cambridge, MA 02139

Wesley K. Lord and Becky Rose
Pratt & Whitney
East Hartford, CT 06118

ABSTRACT

As the propulsor fan pressure ratio (FPR) is decreased for improved fuel burn, reduced emissions and noise, the fan diameter grows and innovative nacelle concepts with short inlets are required to reduce their weight and drag. This paper addresses the uncharted inlet and nacelle design space for low-FPR propulsors where fan and nacelle are more closely coupled than in current turbofan engines. The paper presents an integrated fan-nacelle design framework, combining a spline-based inlet design tool with a fast and reliable body-force-based approach for the fan rotor and stator blade rows to capture the inlet-fan and fan-exhaust interactions and flow distortion at the fan face. The new capability enables parametric studies of characteristic inlet and nacelle design parameters with a short turn-around time. The interaction of the rotor with a region of high streamwise Mach number at the fan face is identified as the key mechanism limiting the design of short inlets. The local increase in Mach number is due to flow acceleration along the inlet internal surface coupled with a reduction in effective flow area. For a candidate short-inlet design with length over diameter ratio L/D = 0.19, the streamwise Mach number at the fan face near the shroud increases by up to 0.16 at cruise and by up to 0.36 at off-design conditions relative to a long-inlet propulsor with L/D = 0.5. As a consequence, the rotor locally operates close to choke resulting in fan efficiency penalties of up to 1.6 % at cruise and 3.9 % at off-design. For inlets with L/D < 0.25, the benefit from reduced nacelle drag is offset by the reduction in fan efficiency, resulting in propulsive efficiency penalties. Based on a parametric inlet study, the recommended inlet L/D is suggested to be between 0.25 and 0.4. The performance of a candidate short inlet with L/D = 0.25 was assessed using full-annulus unsteady RANS simulations at critical design and off-design operating conditions. The candidate design maintains the propulsive efficiency of the baseline case and fuel burn benefits are conjectured due to reductions in nacelle weight and drag compared to an aircraft powered by the baseline propulsor.

NOMENCLATURE

$A_{fan\,face}$, A_{HL}	Fan face area, inlet highlight area
A_0	Streamtube capture area
AoA	Engine angle-of-attack (relative to rotational axis)
a, b	Semi-diameter of super-ellipse describing inlet LE
BPR	Bypass ratio
D, D_{max}	Fan rotor, maximum nacelle diameter
D_{nac}	Nacelle external drag
FPR	Fan pressure ratio
h_t	Stagnation enthalpy
i	Leading edge incidence
K_n	Body force coefficient
L	Inlet length
LE	Leading edge
m, n	Exponent in super-ellipse describing inlet LE
M, M_{is}, M_x	Absolute, isentropic, axial Mach number
MFR	Inlet mass flow ratio
p, p_t	Static pressure, absolute stagnation pressure
P_{core}	Equivalent power in core exhaust
P_{fan}	Power input to fan bypass
P_{shaft}	Shaft power
r	Radial coordinate
R	Rotor tip radius
T_{net}	Net thrust
V_0, V_{jet}	Flight velocity, core jet velocity
w	Mass flow
w_c	Corrected flow
x	Axial coordinate
β	Relative flow angle
γ	Inlet leading edge orientation
η_{fan}	Fan rotor adiabatic efficiency
η_{prop}	Engine propulsive efficiency
θ	Circumferential coordinate
π_{inlet}	Inlet stagnation pressure recovery
ρ	Density
Ω	Rotor rotational speed

BACKGROUND & INTRODUCTION

Next-generation turbofan engine designs for commercial transport aircraft seek higher bypass ratios (BPR) and lower fan pressure ratios (FPR) for improved fuel burn and reduced emissions and noise [1-4], increasing fan bypass stream propulsive efficiencies and enabling higher overall pressure ratios and turbine inlet temperatures [4]. In addition, significant cabin and far-field noise benefits can be achieved by potentially avoiding buzz-saw noise, reducing fan broadband and rotor-stator interaction noise, and enabling steeper take-off profiles due to excess thrust capability [5-7].

Reductions in fan pressure ratio can be realized for example through geared low-speed fans. First-generation geared turbofan engines with BPR = 12 and FPR ≈ 1.4 for short-to-medium range aircraft are expected to deliver fuel burn reductions of up to 16 % compared to current engines in the same thrust segment [8]. From engine cycle analysis, second-generation geared turbofan engines with pressure ratios of 1.3 and lower are expected to offer fuel burn benefits of up to 25 % [1-2, 9-10]. The gear system allows the fan rotor and the low-pressure compressor (LPC) and low-pressure turbine (LPT) to operate at different rotational speeds, reducing fan noise and LPC and LPT stage counts and weight [11].

High bypass and low fan pressure ratios require large engine diameters, increasing the engine contribution to overall drag and compounding adverse installation effects on the wing aerodynamics. A paradigm shift in nacelle design and engine integration is required to realize the potential fuel burn benefit of low-FPR propulsors [4, 9, 11, 12-13]. Specifically, shorter inlet and exhaust ducts are needed to minimize the impact of large diameter fans on nacelle weight and drag. However, short inlets have reduced internal diffusion capability, and inlet flow distortion effects can be exacerbated leading to reduced rotor performance. A sensitivity analysis for a candidate second-generation geared low-FPR propulsor suggests a 1 % reduction in fan efficiency corresponds to a 0.85 % reduction in engine propulsive efficiency, whereas a 1 % reduction in total nacelle drag results in a 0.07 % increase in propulsive efficiency [14]. Shorter inlets can also lead to fan and LPC stability challenges and aero-mechanical issues, and yield reduced fan noise attenuation and shielding opportunities.

Current engines for short-to-medium range civil transport twin-engine aircraft feature inlet L/Ds between 0.65 and 0.85. For long-range aircraft, the L/D range is typically 0.5 to 0.65 [8]. In the present paper, a baseline configuration at the low end of current design practice is defined. The baseline propulsor is based on an advanced, geared fan stage with a BPR of 20 and a non-axisymmetric inlet with $L/D = 0.5$ and 5° droop to align the inlet highlight with the wing upwash, as illustrated in Fig. 1. A thin upper inlet lip mitigates nacelle wave drag at high flight Mach numbers and the thicker lower lip allows separation-free operation at high angles-of-attack (AoA). The baseline configuration includes the pylon and bifurcation in the bypass duct and the core in- and outflows are also modeled. To allow the rotor to operate at peak efficiency at all critical operating conditions, up to 25 % fan nozzle area control is required.
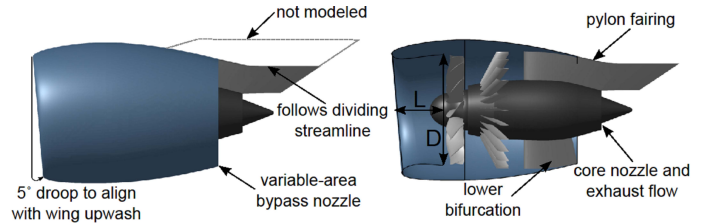

Fig. 1: Baseline propulsor with $L/D = 0.5$.

This paper is aimed at determining the potential of short-inlet configurations to reduce nacelle drag without jeopardizing fan and compressor stability. The emphasis is on the aerodynamic propulsor performance including inlet-fan and fan-exhaust nozzle interactions.

The performance assessment of a candidate short-inlet configuration defined in this paper demonstrates that nacelle external drag reductions of 15 % and more are possible by shortening the inlet from $L/D = 0.5$ to $L/D = 0.19$, enabling significant improvements in propulsor performance. However, the sensitivity analysis highlights the importance of limiting rotor incidence distortion and rotor losses in short-inlet designs since any benefits from nacelle drag reductions can be outweighed by the impact of fan efficiency penalties. The trade-off between reductions in nacelle drag on the one hand and reductions in fan efficiency on the other hand is one of the key aspects in the developed design strategy for short inlets and nacelles.

Previous Work. The onset of flow separation during steep climbs at take-off (T/O) is one of the critical considerations in the design of subsonic inlets [15-16]. Conventional methods that determine whether the inlet flow is separated are based on through-flow nacelle models which do not account for the effects induced by the rotor including blockage, swirl, and suction [17]. Including the influence of the rotor and stator in the design of the inlet and nozzle is important as the favorable pressure gradients in the inlet, induced by the rotor suction, can increase the separation-free AoA [18-20]. Also, determining the distortion transfer and stability margin requires modeling the complete fan stage. In the past, various studies using potential flow [21], Euler [22-24], and two-dimensional actuator disk models in a Navier-Stokes solver [25] were conducted to simulate the flow through the fan rotor. However, potential flow simulations are limited to subsonic, non-separated flows. Euler calculations can be used in sub- and supersonic conditions but are also limited to attached flows. The 2D actuator disk model does not capture swirl effects and usually requires the input of prescribed stagnation pressure and temperature changes across the rotor. Direct full-annulus unsteady CFD simulations are required to capture the once-per-revolution inlet distortion patterns and distortion transfer through the fan stage. For example, such a simulation of a fan stage plus pylon configuration requires about 50 million grid points and needs to be run on 100 or more processors for reasonable computation times [26]. The large computational resources associated with

2

full-annulus URANS calculations render the direct CFD approach unsuitable in the design phase or the parametric exploration of coupled inlet-fan systems. In this work, a body force method is developed to assess the performance of novel nacelle configurations [14]. In this approach, the fan rotor blade row is replaced with a force field, which produces the same pressure rise and flow turning.

Using a three-dimensional (3D) transonic potential flow method in combination with a 3D boundary layer method, Zimbrick and Colehour [27] present inlets for fan bypass ratios of up to 17.5 requiring several new features such as variable pitch, geared fans, and variable-area nozzles. Larkin and Schweiger [20] discuss a configuration featuring an external plug with a center body extending forward of the inlet highlight plane, which enabled a reduction of the inlet length to an L/D of 0.2. Experimental results show separation-free operation at up to 12° larger angles-of-attack than the conventional inlet but with indicated high-speed performance penalties.

In a more recent study by Daggett [28], the integration of advanced technology engines developed under the NASA Ultra Efficient Engine Technology (UEET) program on advanced technology airframes was evaluated and compared to datum baseline configurations for several aircraft size categories. For large aircraft (Boeing 747 size), a 30 % increase in nacelle drag was estimated when replacing a baseline turbofan with $BPR = 7$ and 125" fan diameter with a candidate geared turbofan with $BPR = 14.3$ and 152" diameter. In a follow-up analysis [29], the integration of several high-bypass ratio powerplant candidates on a Boeing 777 aircraft was assessed. Fuel burn reductions of up to 16 % were estimated for an $FPR = 1.45$ propulsor with a geared fan. It was concluded that a lower pressure ratio fan ($FPR = 1.32$) with variable-area nozzle (VAN) capability was not required as the additional fuel efficiency benefits were offset by increased drag of the larger-diameter nacelle. However, the nacelles in both studies featured conventional inlets and were not optimized. The results highlight the need for the design of new nacelle concepts to limit nacelle and drag penalties due to larger diameter nacelles and to take advantage of the potential for additional fuel burn reductions in propulsors with fan pressure ratios lower than 1.45.

Scope of the Paper. The objectives of this paper are to: (1) explore the uncharted design territory of short inlets and nacelles for low-FPR propulsors, (2) identify and quantify the aerodynamic mechanisms limiting the design of short inlets, and (3) provide a short-inlet design strategy and design guidelines. The hypothesis is that there is an optimum L/D range somewhere above 0.2 and below 0.5 for best propulsive efficiency mainly governed by two competing effects: as the inlet length is shortened, the fan rotor adiabatic efficiency starts to drop off due to increased incidence distortion, while the external nacelle drag is reduced and inlet pressure recovery is increased, improving propulsive efficiency.

To assess this hypothesis, an integrated inlet and nacelle design framework was developed, coupling a spline-based tool for the definition of inlet and nacelle surfaces with a body-

force-based approach for the fan rotor and stator blade rows. This new capability captures the inlet-fan and fan-exhaust interaction and flow distortion at the fan face. The paper shows that an L/D of 0.25 represents the shortest possible inlet length for achieving propulsive efficiency benefits over the long-inlet baseline case with $L/D = 0.5$. For further reductions in inlet length, the fan efficiency penalties due to the increased interaction between the rotor and a local region of high Mach number and the reduced flow straightening through the short inlet outweigh the benefits from additional nacelle drag reductions.

SHORT-INLET DESIGN STRATEGY

A preliminary performance assessment of inlet designs with L/D as low as 0.02 suggested that inlets with length lower than approximately $L/D = 0.2$ do not achieve the propulsor performance levels of the long-inlet baseline configuration with $L/D = 0.5$ at cruise and incur prohibitive fan efficiency penalties at off-design conditions. Consequently, the design strategy and guidelines presented in this section are focused on inlet L/Ds of 0.2 and above. The details of the preliminary parametric inlet length study are presented in [14].

Design Requirements. The design requirements for inlets and nacelles are set by trades between the propulsor performance at cruise and at multiple off-design operating conditions. Due to the computational cost of full-annulus CFD simulations, it was not practical to consider the entire list of operating conditions in this work. Instead, only the conditions expected to limit the design of short inlets and due to nacelle drag penalties or increased incidence distortion, jeopardized fan and LPC stability, or exacerbated fan aero-mechanical challenges, were considered. These are listed in Table 1.

Table 1: Critical operating conditions.

|	Condition	Mach number M_0	Altitude h_0	Engine angle-of-attack AoA
1	Cruise ADP	0.8	35,000 ft	5°
2	Wing C_{Lmax}	0.25	14,000 ft	29°
3	Max. cross-wind (30 kts)	0.0442	SL + 15 C	(90°)
4	Take-off rotation	0.25	SL + 15 C	17°
5	Take-off level	0.25	SL + 15 C	0°

At the cruise aerodynamic design point (ADP), the engine is at $AoA = 5°$ due to the wing upwash. The off-design wing C_{Lmax} condition features the largest AoA, which the engine can be subjected to in flight. At the cross-wind condition, inlet flow separation and high levels of rotor incidence distortion are the primary concerns. While the wing C_{Lmax} operating condition is important in the certification process, it is not encountered in a typical flight mission. Thus, the T/O rotation condition is included to quantify the fan efficiency penalties due to increased inlet flow non-uniformities. An additional operating condition with level inflow was defined to address the propulsor performance just before T/O rotation since the flow

was found to potentially separate at the upper inlet lip of short inlets with thin profiles.

The design criteria include limits for the maximum external Mach number to avoid large wave drag penalties at cruise. At off-design, the criteria include fully attached inlet flow and constraints for the minimum static pressure coefficient in the inlet to maximize inlet stagnation pressure recovery and to mitigate rotor incidence distortion [9]. Slender, streamlined inlet and nacelle shapes are therefore required to mitigate cruise wave drag. Thicker inlet lips with round leading edges are needed for separation-free inlet performance and low inlet flow distortion levels at low-speed, high-AoA conditions.

Design Challenges. The streamlines dividing internal and external flows are depicted in Fig. 2 for a short-inlet design with L/D = 0.19. The streamtube capture area is smallest at cruise, the mass flow ratio, MFR, defined as the ratio of streamtube capture A_0 and inlet highlight area A_{HL}, is smaller than one, MFR_{cruise} < 1, and the stagnation point is located on the inside of the inlet lip. At low-speed conditions such as wing C_{Lmax} or T/O rotation, the streamtube capture area grows, the mass flow ratio is larger than one, $MFR_{low-speed}$ > 1, and the stagnation point shifts to the nacelle external surface.
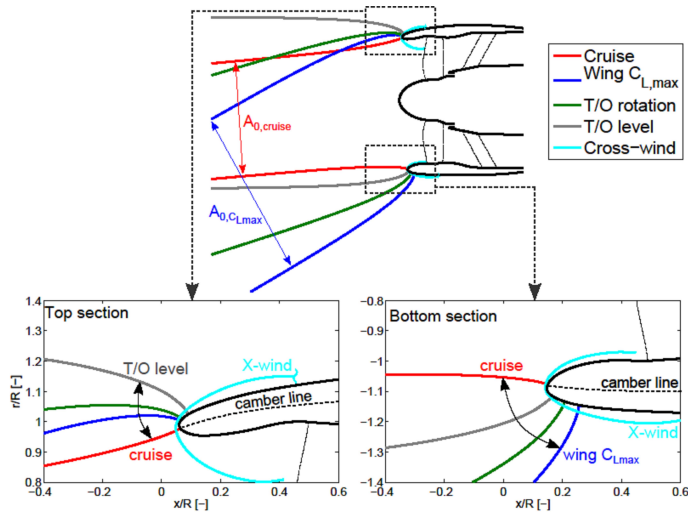
Fig. 2: Dividing streamlines between internal and external flows for a candidate short-inlet design with L/D = 0.19.

Relative to the other operating conditions, the free-stream Mach number is lowest at the cross-wind condition, $M_{0,X-wind}$ = 0.044, and the streamtube capture area is largest. Two streamlines close to the lip are shown at the top and bottom of the nacelle, respectively, for the cross-wind condition. In conventional inlet designs, the requirement for attached flow in the inlet at the cross-wind condition is a driver for increased lip thickness around the entire circumference. Because the top section must be thin to mitigate drag penalties at cruise, separation-free inlet flow could not be satisfied for the candidate short-inlet design with L/D = 0.19. For inlets with L/D smaller than about 0.25, flow control such as blow-in doors

in the inlet may be required to reduce separation and alleviate inlet flow distortion.

At cruise, the strength of the shock on the front nacelle surface is governed by the inlet lip and nacelle external shapes downstream of the stagnation point. Limiting the shock strength and wave drag penalties requires aligning the outer nacelle geometry with the incoming dividing streamline and limiting the curvature along the outer portion of the inlet lip. If the 2D nacelle profiles at the top and bottom are viewed as airfoils, the camber angle should be chosen such that the front inlet and nacelle shape is oriented towards the incoming streamline and the local angle-of-attack on the airfoil is minimized, as indicated on the bottom in Fig. 2. The flow upwash due to the wing potential field results in a 5° AoA of the free-stream relative to the engine axis of rotation. As a consequence, the top section is at a larger local angle-of-attack than the bottom section and therefore requires a larger camber angle to limit the over-speed on the nacelle external surface.

While short-nacelle designs with positive camber angles promote low Mach numbers on the nacelle external surface, the outward shift in the stagnation point for low-speed conditions requires reduced camber angles or "un-cambered" airfoil profiles to limit the flow acceleration along the inlet internal surface and provide for separation-free inlet flow. The T/O level operating condition is representative of a low-speed condition with low AoA. At the top section, the stagnation point shift between off-design and cruise is largest for T/O level. The stagnation point moves outward and downstream on the nacelle external surface and the flow accelerates around the inlet lip. In short inlets with thin profiles, the flow tends to separate in the inlet. The requirement for attached inlet flow and low rotor incidence distortion at the T/O level condition sets the lower limit on the inlet thickness.

At the bottom section, the shift in the stagnation point between off-design and cruise is largest for the wing C_{Lmax} condition with AoA = 29°. Compared to the top section, an increased lip thickness is required for separation-free inlet flow and limited flow acceleration around the inlet lip at off-design. Reducing the airfoil camber angle proved to be an effective design technique for determining the required inlet lip orientation for separation-free inlet flow at wing C_{Lmax} while limiting external flow acceleration at cruise.

Compared to the design of long inlets, an additional challenge unique to short inlets arises due to the continuous decrease of the flow area throughout the inlet, illustrated in the top plot of Fig. 3. In the long inlet, the reduction in flow area between the highlight and throat is followed by an increase up to the spinner leading edge (LE) location. As the spinner thickness grows, the flow area decreases up to the fan face. The average Mach number reaches a local maximum at the throat, as shown in the center plot, and the reduction in the flow area between the highlight and inlet throat is accompanied by a flow acceleration approaching the fan face, where $M_{fan\ face}$ = 0.63. In combination with the inflow at AoA, the local flow acceleration along the bottom inlet surface is at a maximum close to the throat, as indicated by the isentropic Mach number distribution

4

in the bottom plot. This local maximum is reached far upstream of the rotor, as illustrated later in this paper in the discussion of the candidate short-inlet designs. While the averaged Mach number is highest at the fan face, the radial and circumferential flow non-uniformities caused by the AoA inflow are reduced at the fan face due to the flow straightening through the inlet.
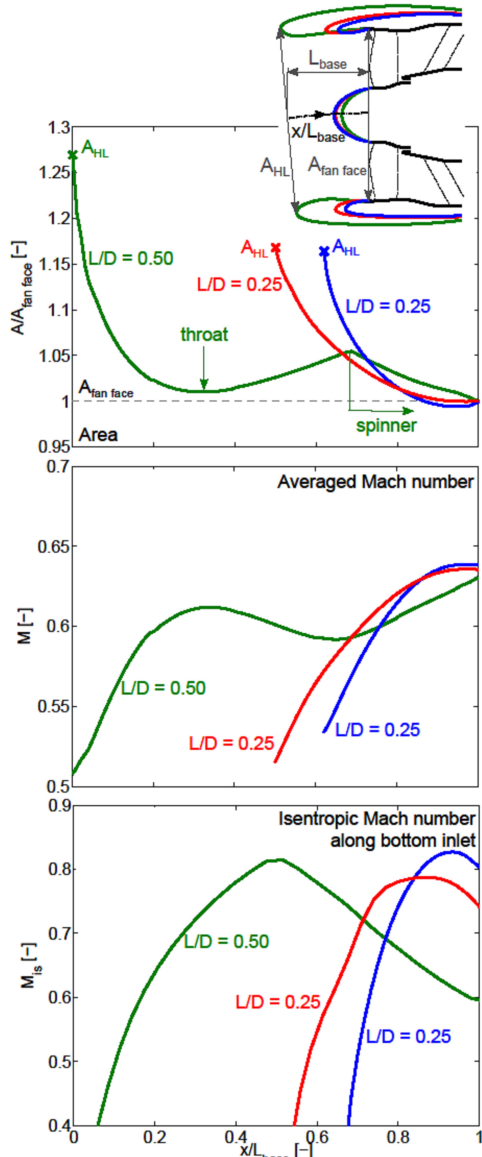

Fig. 3: Distributions of inlet area (top) and averaged Mach number (center) through the inlet and isentropic Mach number along bottom inlet (bottom) for *L/D* = 0.5, *L/D* = 0.25, and *L/D* = 0.19 propulsors at cruise.

In short inlets with extended spinners, the flow area monotonically decreases throughout the inlet and the location of the maximum flow acceleration near the shroud is close to the location of the maximum averaged Mach number at the fan face, as depicted in the center and right-hand plots in Fig. 15. Due to the proximity of the region of high Mach number to the

fan face, incidence distortion is enhanced, leading to increased rotor losses.

Incidence Distortion Mechanisms. The rotor incidence distortion and the distortion transfer through the fan stage are governed by the following mechanisms: (1) the interaction of the fan stage with the pylon and bifurcation upstream influence and (2) the interaction of the rotor with the non-uniform inflow (with AoA > 0) through the 3D inlet. The relative importance of these mechanisms in the long-inlet baseline propulsor at cruise was quantified by carrying out URANS simulations for the following three cases, as illustrated in Fig. 4:

1. The first simulation includes the entire propulsor. Both the non-uniform inflow with *AoA* = 5° through the non-axisymmetric inlet and the pylon and bifurcation are modeled.
2. The impact of the back pressure distortion generated by the pylon and bifurcation potential field on the fan performance is quantified by modeling the internal flow through the bypass duct at uniform inflow.
3. The contribution of the non-uniform inflow is determined by removing the pylon and bifurcation geometries from the computational model.
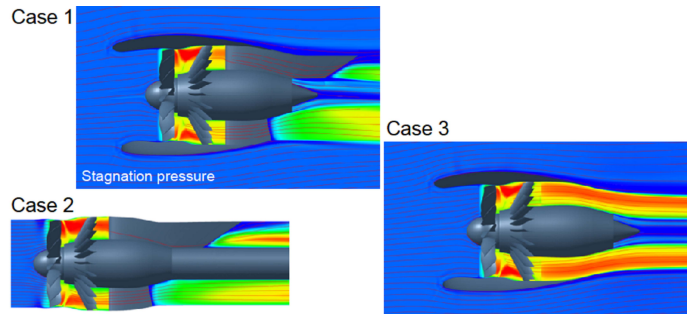
Fig. 4: Overview of computational approach to quantify the incidence distortion mechanisms in the baseline propulsor.

The distributions of the stagnation pressure relative to the mass-averaged value downstream of the rotor, $(p_t - p_t^M)/p_{t0}$, are plotted along the circumference mid-span in Fig. 5. In simulations 1 and 2, the increased rotor back pressure due to the pylon leads to an increase in the rotor work input and a local increase in the stagnation pressure near $\theta = 0°$, 360°. Compared to the local increase in the stagnation pressure due to the pylon potential field, the bifurcation upstream influence causes a smaller local increase near $\theta = 180°$. In case 3, the variation is approximately sinusoidal with reduced stagnation pressure over the first half of the rotor revolution due to reduced incidence and increased stagnation pressure over the second half due to increased incidence.

Superposition of the stagnation pressure variations from cases 2 and 3 agrees with the full-domain result (case 1) to within 0.15% of the mass-averaged stagnation pressure, p_t^M/p_{t0}, suggesting that the mechanisms contributing to the distortion transfer are de-coupled and reductions in the incidence and

5

stagnation pressure distortions can be achieved by addressing the mechanisms independently. The stagnation pressure variations due to the pylon upstream influence are up to twice as high as the variations induced by the non-uniform inflow, indicating that pylon upstream influence is the dominant mechanism for the distortion transfer in the baseline propulsor at cruise. In shorter inlets, the relative contribution from the non-uniform inflow increases. While the impact of the pylon potential field can be alleviated by tailored FEGV designs, designing inlet shapes for reduced incidence distortion is particularly important in short-inlet configurations.
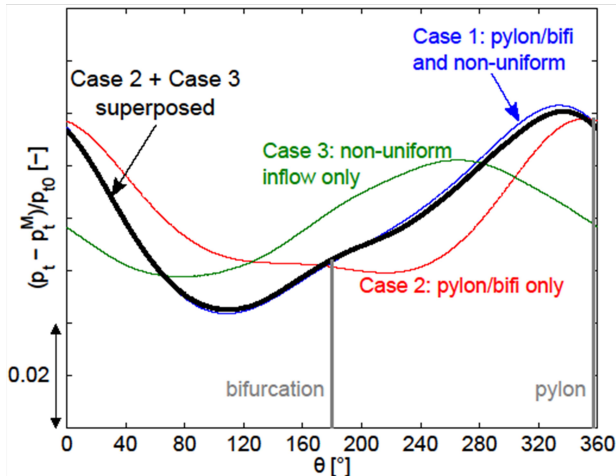

Fig. 5: Superposition of the contributions from non-uniform inflow and pylon/bifurcation upstream influence to the stagnation pressure variation downstream of the rotor at mid-span in the baseline propulsor with L/D = 0.5 at cruise.

Inlet and Nacelle Design Approach. Since there are considerable differences in the requirements on the top and bottom sections of the inlet and nacelle, the first step of the design approach is based on independently addressing the top and bottom profiles.

The shape of the top inlet and nacelle section is critical for limiting the external flow acceleration and wave drag at cruise. Supercritical airfoil shapes provide for low drag due to reduced flow acceleration on the upper surface and an approximately supersonic plateau, followed by a weak shock downstream of mid-chord. The design philosophy behind supercritical airfoils is described for example in [15] or [30]. The design of nacelles which take advantage of the supercritical airfoil characteristics are discussed for example by Langley [31] or Barber et al. [32]. In the current work, supercritical airfoils serve as the starting point for the design of the top inlet and nacelle sections.

For an inlet with L/D = 0.19, the design approach is illustrated in Fig. 6. Based on the constraints on the maximum nacelle diameter, the thickness of the supercritical airfoil shape is selected. The present example shows the NASA SC(2)-0710 airfoil [30] with 10 % thickness. The internal shroud geometry is defined as part of the fan stage design and the nacelle boattail radial location is set by the required nozzle area at the cruise design point. In the first step, the aft part of the airfoil is

modified to satisfy the constraints on the fan case and boattail geometry. The modified geometry is shown in red in Fig. 6.

The second step is the modification of the inlet internal shape and the front part of the nacelle external geometry. The camber line geometry of the preliminary design must be aligned with the incoming stagnation point streamline to reduce the over-speed in the external flow. Shaping the nacelle external geometry is critical in the design process since small changes in the curvature can have large effects on the surface pressure distribution and the shock strength at cruise. Reducing the thickness of the inlet lip is effective in further alleviating the over-speed at cruise. However, a smaller inlet lip thickness results in an increase in the local over-speed along the inlet at low-speed, off-design conditions and enhances the incidence distortion. For the short inlet shown in Fig. 6, the minimum inlet lip thickness was set by the requirement for fully attached inlet flow at the T/O level operating condition.
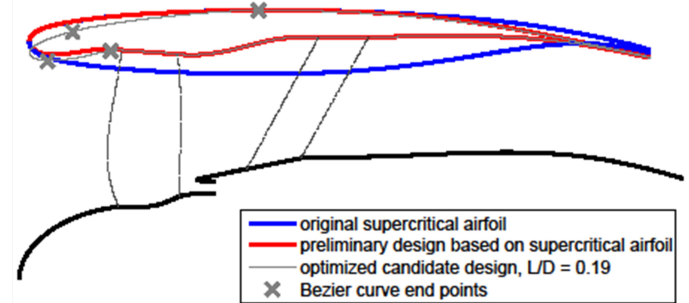

Fig. 6: Example for top inlet and nacelle shape description based on supercritical airfoil.

In contrast to the top part of the inlet and nacelle, the bottom part requires a thicker inlet lip to avoid flow separation and to mitigate rotor incidence distortion at low-speed, high-AoA conditions. In short inlets, the shape of the inlet also plays an important role in reducing the region of high Mach number over the outer span at cruise and limit fan efficiency penalties.

An elliptical description of the bottom inlet LE geometry was implemented to determine the important parameters for limiting external flow acceleration at cruise and over-speed along the inlet internal surface at the wing C_{Lmax} operating condition. The parametric description is depicted in Fig. 7 for an inlet with L/D = 0.25. The inlet and nacelle LE shape is split into two sections on either side of the inlet highlight location. Each section is described by a super-ellipse with ellipse semi-diameters a and b and exponents m and n. The orientation of the profile camber line at the LE relative to the axial direction is controlled by the angle γ. For a candidate design with a given L/D, the parametric description of the bottom inlet allows optimizing, for example by conducting a parameter study for the orientation γ and the LE thickness. By increasing γ, the camber line is more aligned with the inflow at the low-speed, high-AoA conditions and the highlight area is increased. As a result, the over-speed along the inlet internal surface is reduced and the maximum Mach number at the fan face decreases. The downside of increasing γ is the increase in the maximum Mach number on the external surface at cruise.
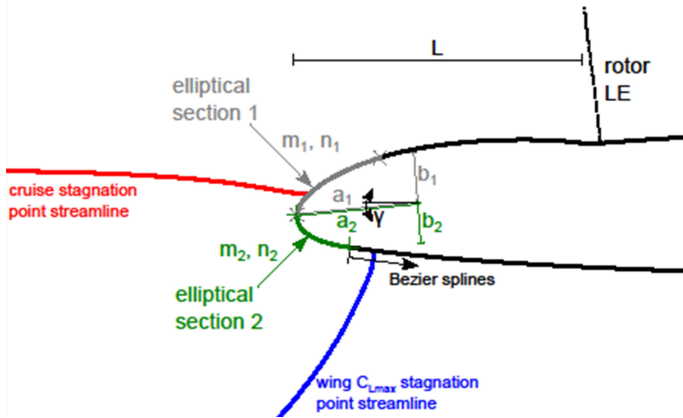
This document has been publicly released   6   Copyright © 2014 by ASME

Fig. 7: Parametric description of bottom inlet leading edge.

In addition to the inlet and nacelle shapes, the spinner geometry can play an important role in the propulsor performance at both design and off-design operating conditions. In general, shortening the inlet requires an increase in the axial spinner length to reduce the incidence distortion near the hub. Spinner designs extending forward of the inlet highlight plane enable performance benefits at cruise by moving the stagnation point outward and alleviating the over-speed along the nacelle external surface. However, that same outward shift in the stagnation point exacerbates the over-speed along the inlet internal surface at low-speed conditions, resulting in increased rotor incidence distortion levels. A detailed assessment of unconventional spinner shapes is given in [14]. The short-inlet propulsors discussed in this paper feature conventional spinner designs similar to the shape included in the baseline configuration, as shown for example at the top in Fig. 3.

INLET AND NACELLE DESIGN METHOD

An overview of the integrated inlet and nacelle design framework is provided next. The key features are the body force representations of the fan rotor and FEGV blade rows and a spline-based approach to define the inlet and nacelle surfaces.

Bezier splines were selected to describe the top and bottom two-dimensional sections. Each spline consists of a series of four Bezier curves, as shown in Fig. 8. The inlet and the front part of the nacelle are non-axisymmetric, with different Bezier curves at the top and bottom. Downstream of the maximum nacelle diameter axial location, the nacelle surface is axisymmetric and the Bezier curves at the top and bottom are the same. Each Bezier curve is defined by a series of control points which do not necessarily lie on the resulting Bezier curve, except for the two end points. At the start (or end), a given Bezier curve is always tangent to the line between the start point and the next control point (or the end point and the second-to-last control point). This characteristic feature is used to ensure tangency continuity at the joints between two Bezier curves. Matlab was used to implement the spline-based approach and a capability was set up to interactively change the Bezier curve shapes by moving control points. The ability to modify the different pieces by moving control points without

affecting neighboring curves is one of the main advantages of the developed approach.

For each inlet and nacelle section, the half-annulus surface description is computed as a function of the circumferential coordinate θ by linearly interpolating between the top and bottom sections and adding a sinusoidal dependence in θ to ensure tangency and curvature continuity at $\theta = 0$ and $\theta = \pi$.
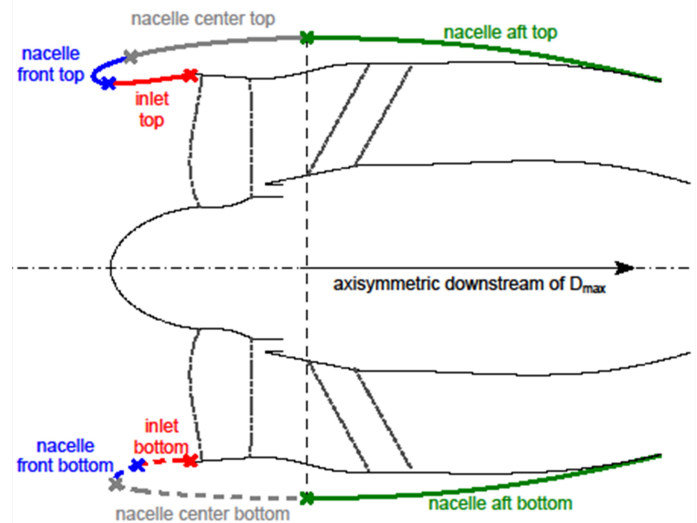

Fig. 8: Piecewise inlet and nacelle geometry definition using Bezier curves.

Body force representations of the rotor and stator blade rows were determined, as described in the next section below, and full-annulus body force simulations were used during the inlet and nacelle design process due to their low computational cost. Once a candidate short-inlet design was finalized, URANS simulations including the discrete blades were carried out to provide a high-fidelity performance assessment. The commercially available software package Numeca FINE/Turbo [33] was used for body force and URANS simulations. In all simulations, turbulence closure was achieved through the use of the Spalart-Allmaras one-equation turbulence model [34].

The design framework can only be effectively used in the design process and in parametric studies if low turn-around times for setting up and running full-annulus 3D simulations are achieved. Each design is evaluated at multiple operating conditions, with each operating condition requiring a different grid due to changes in the variable-area nozzle settings. To limit computational cost, a modular grid topology was established and the grid generation was automated using Numeca's scripting capabilities. The grid modules consist of multi-block structured hexahedral grids. The first module includes the internal rotor and stator domains. Pylon and bifurcation domains make up the second component. The third grid module consists of the inlet and external nacelle domains within two nacelle diameters around the engine. The final component includes the external far-field domains. For the cruise, wing C_{Lmax}, and T/O operating conditions, the far-field module is cylindrical and extends 50 nacelle diameters radially and

7

axially upstream and downstream of the engine to accurately capture the inlet streamtube at low-speed conditions. At the cross-wind condition with $M_0 < 0.05$, an additional domain extension up to 100 nacelle diameters in each direction was required to capture the inlet streamtube and the domain shape was changed to a rectangular cuboid. Since the emphasis was on determining inlet flow separation and its impact on fan performance in the short-inlet candidate designs, the ground plane is not included in the computational model at cross-wind and the formation of an inlet vortex is not captured.

In the URANS assessment, the computational mesh features three grid levels with 3.125 (coarse), 25 (medium), and 200 (fine) million cells, respectively. The medium grid level is used here to limit computational cost. In general, about 100,000 iterations were required to reach a settled unsteady flow solution. Details on the nacelle design framework, the meshing strategy, the computational setup of the URANS calculations, and the results of grid convergence studies can be found in [14].

Engine propulsive efficiency is defined here as the performance metric to measure the conversion of shaft power into propulsive power minus the lost power due to nacelle drag:

$$\eta_{prop} \triangleq \frac{\text{prop. power - lost power due to nacelle drag}}{\text{shaft power}}$$
$$= \frac{(T_{net} - D_{nac})V_0}{P_{shaft}} \quad (1)$$

In Eq. (1), the nacelle drag is defined as the drag from the external nacelle surfaces, consisting of skin friction and pressure components. The engine propulsive efficiency η_{prop} captures both the changes in the nacelle aerodynamic performance due to variations in the external shock strength or surface area and changes in the fan stage performance due to variations in incidence distortion and distortion transfer through the bypass duct. The engine propulsive efficiency is associated with both the control volume CV I for the bypass flow, shown in green in Fig. 9, and the control volume CV II for the external flow, shown in blue in Fig. 9.
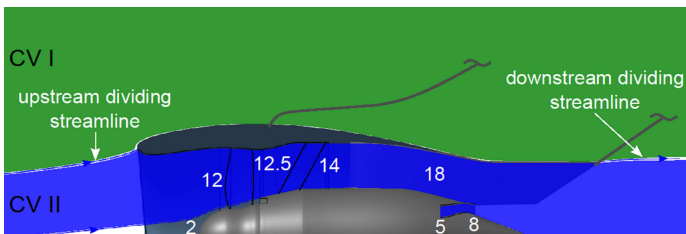
Fig. 9: Control volume definition for calculation of engine propulsive efficiency.

The shaft power consists of the power input to the fan bypass, P_{fan}, and the equivalent power in the core exhaust on a closed cycle basis, P_{core},

$$P_{shaft} = P_{fan} + P_{core}$$
$$= w_{12}(h_{t12.5} - h_{t12}) + w_5 \frac{1}{2}V_{jet}^2 - w_2 \frac{1}{2}V_0^2 \quad (2)$$

In Eq. (2), the stagnation enthalpy rise through the rotor is denoted by $h_{t12.5} - h_{t12}$, with stations 12 and 12.5 up- and downstream of the fan rotor in the bypass stream, respectively, as marked in Fig. 9. The mass flow through the bypass duct is given by w_{12}, and w_2 and w_5 are the core inlet and core exhaust mass flows, respectively. The core jet velocity downstream of the propulsor is denoted by V_{jet}.

A control volume approach is adopted to determine the net thrust minus nacelle external drag, $T_{net} - D_{nac}$, from the results of full-annulus body force or URANS simulations. The detailed approach and the computation of the total power input needed to calculate engine propulsive efficiency are given in [14].

FAN STAGE BODY FORCE MODEL

The physical effects of turbomachinery blades on the flow are due to pressure and viscous forces at the solid surfaces. The fundamental idea behind the body force modeling approach is to redistribute the blade forces in the circumferential direction such that they generate the same stagnation pressure rise and flow turning as the discrete blades. Individual blades exerting surface forces on the fluid are not captured. Instead, an appropriate body force distribution is used to simulate the effects of the blades in the bladed regions of the gas path. Replacing the discrete blades with body force distributions leads to simplified grid topologies and significant reductions in grid point counts since fine mesh resolutions near the blade surfaces are no longer needed. The computational domain is an axisymmetric, 3D channel bound by hub and shroud endwalls. The key advantages of the body-force-based approach in the inlet and nacelle design framework are the reductions in computational cost and the possibility for steady simulations without rotor-stator interfaces.

The body force approach to represent the overall characteristics of a blade row was first introduced by Marble [35], who derived formulations for body forces required to produce a given change in swirl (force component normal to the relative flow) and entropy along a streamline (force component parallel to the relative flow). Based on Marble's ideas and a circumferentially passage-averaged body force model, a 3D method for long-scale problems was developed by Gong [36, 37]. One of the main advantages inherent to Gong's approach when compared to previous actuator disk concepts is that the body force source terms are distributed both radially and axially, enabling the method to capture some of the dynamic blade row response to the unsteady flow field, e.g. due to inertial and/or convection effects. Gong's approach was first applied to simulate axial compressor stall inception and distortion transfer. It was later used by Hsiao [17] to determine the rotor effect on inlet flow separation in a powered nacelle simulation at significantly reduced computational cost compared to full-annulus direct CFD simulations.

Due to its capability to capture fan-inlet coupling and distortion transfer, the approach by Gong is the basis for the body force method developed in this work. The key part of the body force approach is developing a formulation for the functional dependence of the force on local flow conditions.

8

This dependence is established through a momentum balance in the blade passage direction and the normal force is assumed to scale with a body force coefficient K_n, which accounts for the effects not captured by the blade passage model and must be determined before a body force simulation can be run. In previous implementations, K_n was computed based on empirical correlations or experimental data at a limited number of spanwise sections only [17, 36]. Experimental data is usually not available in the fan design phase and as observed in [17], inaccuracies can arise in the body force simulations compared to the measured rotor performance if the force distributions are not based on data on the entire blade domain. For improved accuracy over the entire blade domain, the body force coefficient K_n is computed in this work for the first time at every grid point in the rotor and stator domains based on blade force and flow field data extracted from steady, single-passage RANS calculations. Additional modifications to Gong's original approach include a re-formulation of the parallel force to capture the off-design loss generation for operating conditions near stall and choke, which the rotor can experience locally at low-speed, high-AoA off-design conditions, and accounting for radial force and velocity components, which had previously been neglected.

The formulations for normal and parallel body force components provide source terms, which are added to the right-hand side of the governing equations in the swept volume of the blade rows. The body force method was implemented in a custom version of Numeca FINE/Turbo, which enabled access to the local flow quantities and the addition of user-defined source terms to the governing equations. The derivation of the blade passage model, the calculation of body force distributions from steady RANS simulations, and the implementation of the method are discussed in more detail in [14].

Blade metal and aerodynamic blockage are not modeled in the current implementation of the body force method. The fan stage used in this work consists of a low number of thin blades and accounting for blockage was not deemed critical in the inlet and nacelle design studies. Similarly, tip leakage flow is not modeled since the emphasis in the parametric assessment of inlet and nacelle designs is not in the flow details but on the bulk effects and trends. Finally, since there are no discrete blades in the body-force-based approach, viscous wakes cannot be modeled. The losses due to viscous wake mixing downstream of the blade rows are accounted for by adjusting the stator viscous body force in order to match the fan stage performance computed in the steady RANS simulations. While body force calculations were used extensively in the design process, URANS simulations were always carried out as a high-fidelity check of a candidate short-inlet configuration.

CAPABILITIES AND VALIDATION

Results from internal single-passage body force and steady RANS simulations were compared first to validate the capability of the developed body-force-based approach to capture the rotor and stator performance along a speedline and the change in performance for inlet swirl distortion. In a second step, full-annulus calculations for the entire propulsor including the external nacelle flow as shown in Figs. 2 or 9 were carried out to demonstrate that the coupling of inlet flow and rotor and the distortion transfer at high-AoA conditions are captured.

Compared to URANS simulations with high-resolution blade meshes, which required calculating up to seven rotor revolutions until reaching a settled unsteady state, the body force method enabled a reduction in computation times from approximately seven days to one hour per operating condition.

Off-Design Performance. The capability to assess changes in the rotor performance due to changes in the inflow conditions is a key feature of the developed method. Results for the fan efficiency, η_{fan}, are shown in Fig. 10. To demonstrate the robustness of the method to changes in incidence, the rotor performance is presented for no inlet swirl (marked in black), 5° counter-swirl (marked in red) and 5° co-swirl (marked in blue). The body force description was not changed from the baseline case without inlet swirl.
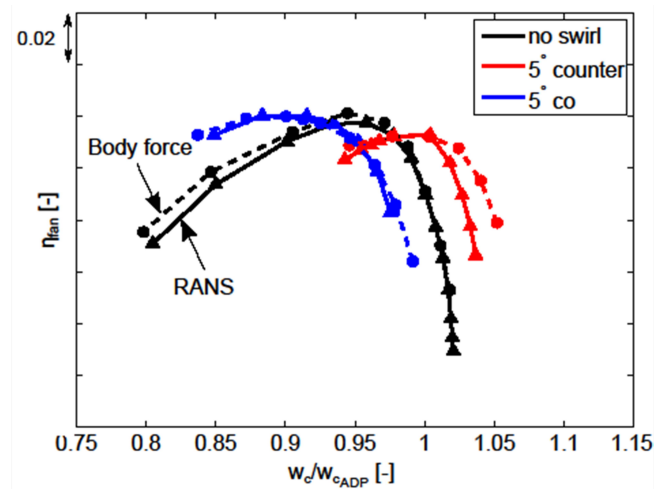
Fig. 10: Fan efficiency for no inlet swirl (black), 5° counter-swirl (red), and 5° co-swirl (blue) at the T/O rotation operating condition. The results from RANS and body force simulations are plotted as solid and dashed lines, respectively. For a single set of body force coefficients, the rotor performance is captured over the entire speedline.

The off-design increase in the blade losses is captured in the body force simulations. In the baseline case without inlet swirl, the stagnation pressure loss is under-predicted at the low-flow conditions, leading to a 0.5% higher efficiency. This discrepancy is attributed to the selection of the body force coefficients in the viscous force description and could be reduced by re-formulating the viscous body force in terms of entropy or dissipation. The method captures the performance changes in the counter- and co-swirl cases. As the corrected flow is increased, the differences increase since blockage effects are not accounted for in the body force simulations.

9
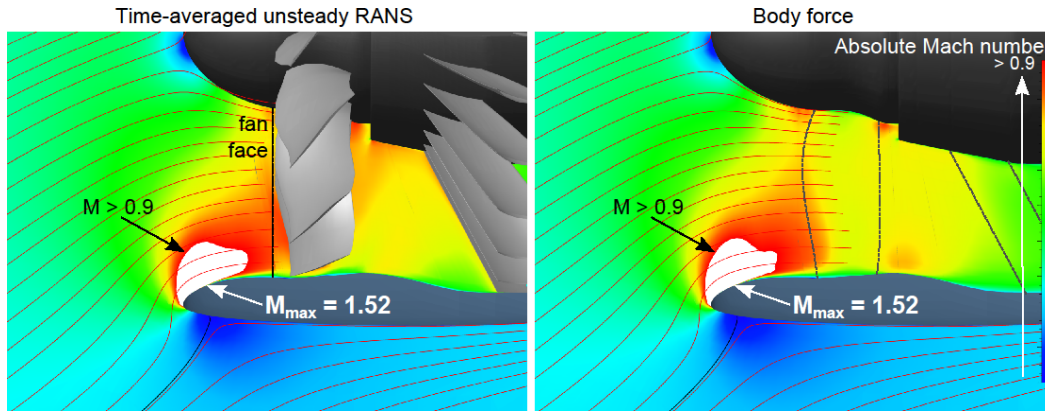
Fig. 11: Candidate short-inlet propulsor with *L/D* **= 0.25 at the wing C$_{Lmax}$ operating condition. Using force distributions obtained from steady, single-passage RANS simulations, the body force method is capable of capturing the interaction between the rotor and inlet flow.**

Inlet-Fan Coupling. The increased interaction between the inlet flow and the rotor plays a critical role in short-inlet configurations and needs to be captured in the body force simulations for the method to be useful in the exploration of short-nacelle concepts. For a candidate short-inlet design, the absolute Mach number distributions in the inlet computed from URANS and body force simulations are shown in the left- and right-hand plots in Fig. 11, respectively, at the wing C$_{Lmax}$ condition. The body force results for streamlines, shape of the accelerated flow region along the inner surface of the inlet, and maximum Mach number inside of this region are in agreement with the time-averaged URANS calculation.
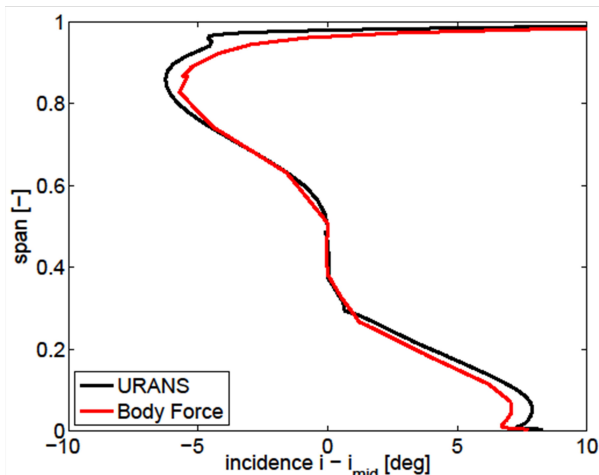
Fig. 12: Spanwise profile of rotor incidence corrected by mid-span value for short-inlet design with *L/D* **= 0.25 at wing C$_{Lmax}$.**

The spanwise profile of rotor incidence is extracted along the fan face location depicted on the left in Fig. 11 and a comparison of the profiles from time-averaged URANS and body force results is presented in Fig. 12. The body force results agree with the URANS data to within 1°, with the highest discrepancies near hub and shroud. At the hub, metal blockage is largest and the upstream influence of the discrete blade results in flow deceleration at the fan face. Since blockage is not captured in the body force simulations,

incidence is under-predicted. Near the shroud, the Mach number is increased due to the flow acceleration around the bottom inlet lip and the rotor operating condition locally shifts towards choke.

Powered vs. Flow-Through Nacelle. To determine the impact of the fan rotor on inlet flow separation at high-AoA conditions, the results of body force simulations (powered nacelle) were compared to a flow-through nacelle calculation for a short-inlet design with *L/D* = 0.25. In the flow-through simulations, the mass flow rate from the simulation with the rotor effect was used as the outflow boundary condition downstream of the stator in the bypass duct. The calculations were performed at the wing C$_{Lmax}$ operating with M_0 = 0.25 and *AoA* = 29°. The distributions of the axial Mach number and the streamlines near the bottom inlet are shown in the left- and right-hand plots in Fig. 13 for the flow-through and powered nacelle simulations, respectively. The inlet flow is separated in the flow-through nacelle, whereas the boundary layer remained attached in the powered nacelle simulation due the favorable pressure gradient induced by the rotor suction near the shroud. The results of flow-through nacelle calculations with reduced AoA indicate that the presence of the rotor increases the separation-free AoA by 4° relative to the flow-through nacelle, which is in agreement with the observations in past numerical investigations [15, 16] and experimental studies [19]. The results underline the importance of capturing the influence of the rotor on the inlet flow in short-inlet designs and demonstrate the capability of the developed body force method to deal with the fan-inlet coupling.
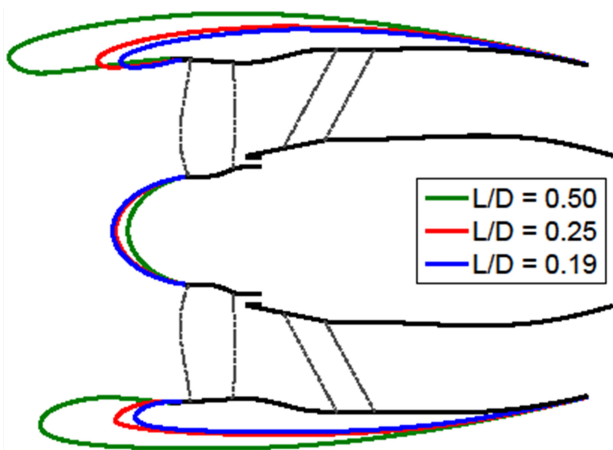
CANDIDATE SHORT-INLET DESIGNS

Inlet and nacelle were parametrically shortened using body force simulations to quantify the trades between reduced nacelle drag and increased rotor efficiency penalties due to enhanced incidence distortion. Based on the results, two candidate short-inlet designs were defined. The first design features an inlet with *L/D* = 0.25. The 2D top and bottom inlet and nacelle shapes of the *L/D* = 0.5 baseline and *L/D* = 0.25 short-inlet configurations are presented in green and red in Fig.

10
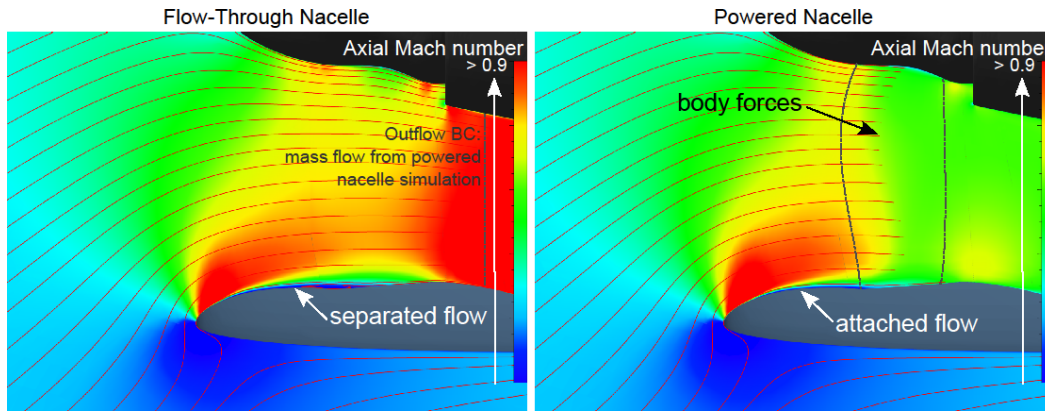
Fig. 13: Candidate short-inlet propulsor with *L/D* = 0.25 at the wing C$_{Lmax}$ operating condition (AoA = 29°). The results for the flow-through nacelle simulation show separated inlet flow (left). Due to the favorable pressure gradient generated by the rotor near the shroud, the inlet flow is attached in the powered nacelle case with body forces in the rotor blade row (right).

14, respectively. As the inlet is shortened, the spinner is extended to enhance flow straightening and limit circumferential incidence variation near the hub. To take advantage of additional reductions in nacelle drag by shortening the inlet beyond *L/D* = 0.25, the performance of an inlet of length *L/D* = 0.19 was quantified. The 2D top and bottom profiles for this design are shown in blue in Fig. 14.

Fig. 14: Top and bottom inlet and nacelle sections for the baseline *L/D* = 0.5 and the *L/D* = 0.25 and *L/D* = 0.19 candidate short-inlet designs.

During the design process of the two candidate short-inlet configurations, surface pressure distributions along the inlet and nacelle were extracted from body force simulations along with maximum Mach numbers at cruise and incidence distortion levels at off-design conditions. Using the developed strategy, 20 to 30 design iterations were performed until inlet and nacelle shapes with acceptable design and off-design performance ($M_{max} \approx M_{max,base}$ at cruise, attached inlet flow and low incidence distortion at off-design) were obtained.

By defining an inlet LE shape which limits the swing in the stagnation point on the bottom inlet between cruise and wing C$_{Lmax}$, the final *L/D* = 0.25 design provides for separation-free flow at the wing C$_{Lmax}$ condition. For an inlet with *L/D* = 0.19,

it was not possible to achieve fully attached inlet flow at the wing C$_{Lmax}$ condition without a sharp increase in the Mach number and the shock strength on the nacelle external surface. Some inlet flow separation at the wing C$_{Lmax}$ condition must be accepted for an inlet length as low as *L/D* = 0.19.

The performance of the candidate short-inlet propulsors at cruise and off-design operating conditions is summarized in Table 2. At cruise, the *L/D* = 0.25 design maintains the baseline propulsor performance to within 0.01 % propulsive efficiency. The nacelle drag is reduced by 16.0 % due to the reduction in the wetted nacelle area but the benefits from the nacelle drag reduction are offset by a fan efficiency penalty of -0.96 % due to the increase in the rotor incidence distortion.

Table 2: Performance overview of L/D = 0.25 and L/D = 0.19 candidate short-inlet propulsors relative to the L/D = 0.5 baseline based on time-averaged URANS solutions.

Condition/Metric	L/D = 0.25	L/D = 0.19
Cruise ADP		
$\Delta\eta_{prop}$	-0.01 %	-0.80 %
ΔD_{nac}	-16.0 %	-17.8 %
$\Delta\eta_{fan}$	-0.96 %	-1.63 %
Wing C$_{Lmax}$		
$\Delta\eta_{fan}$	-1.84 %	-3.94 %
Cross-wind	not	
$\Delta\eta_{fan}$	computed	-1.53 % (*)
T/O rotation		
$\Delta\eta_{fan}$	-1.55 %	-2.48 %
T/O level		
$\Delta\eta_{fan}$	-1.01 %	-1.85 %

(*) with blow-in doors in inlet

The absolute Mach number distributions for the baseline and the *L/D* = 0.25 short-inlet configurations are depicted in the top left and center in Fig. 15, respectively. Limiting the flow acceleration along the nacelle external surface was one of the main objectives in the short-inlet design strategy and the size of the region of supersonic flow along the front part of the upper surface was kept similar while the maximum Mach number at the shock only increased by $\Delta M_{max} = 0.02$.
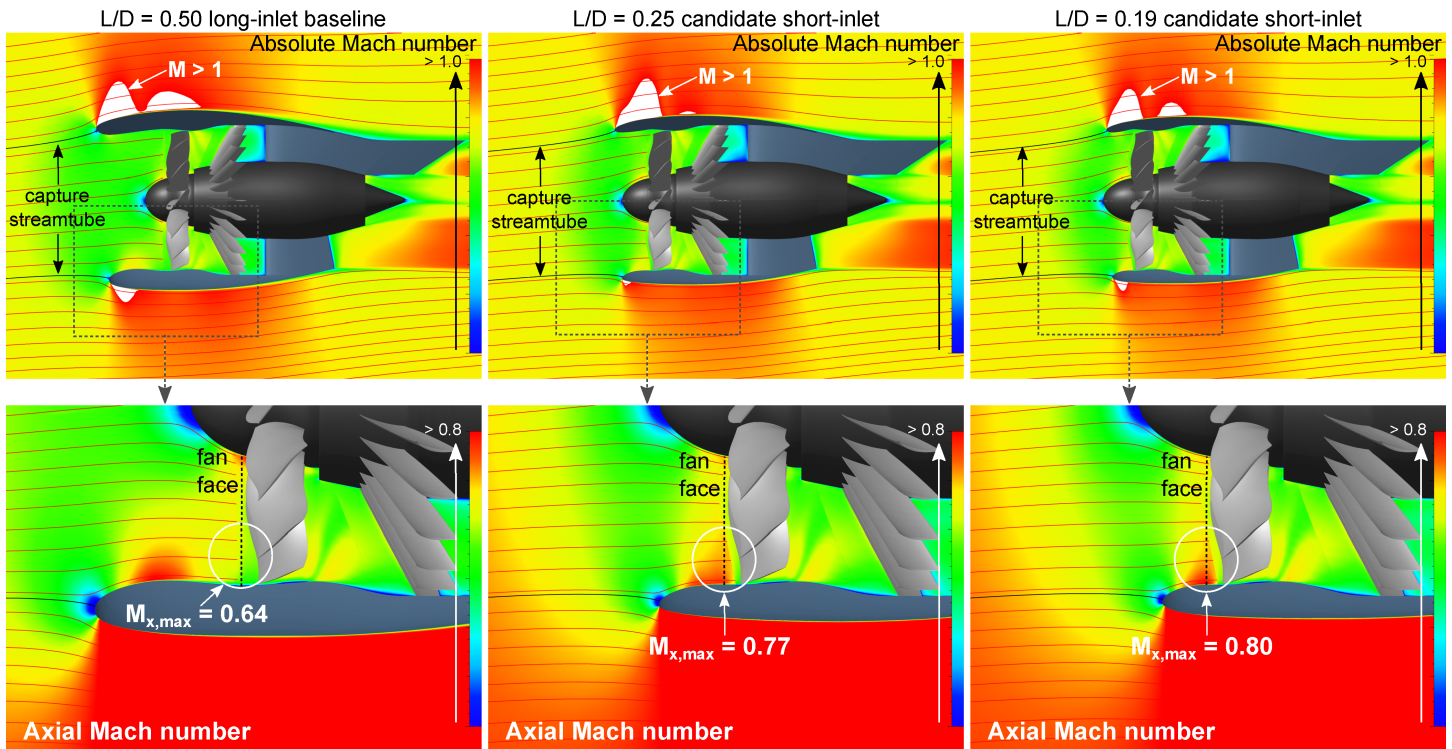
Fig. 15: Mach number distribution (top) and axial Mach number distribution (bottom) for the baseline propulsor (left) and the candidate short-inlet designs with *L/D* = 0.25 (center) and *L/D* = 0.19 (right) at cruise.

The axial Mach number distributions in the inlet flow are presented for the baseline and *L/D* = 0.25 candidate design in the bottom left and center in Fig. 15, respectively. As indicated in the isentropic Mach number distributions in the bottom plot in Fig. 3, there is a region of increased axial Mach number over the outer span at the fan face in the short inlet. The maximum axial Mach number in this region is increased by $\Delta M_{x,max}$ = 0.13. The increase in M_x further reduces the rotor incidence by up to Δi = -5° over the outer span and the local operating point shifts towards choke. The interaction of the rotor with the high Mach number is one of the main reasons for the 0.96 % reduction in fan efficiency relative to the baseline. In addition, the flow straightening through the inlet is reduced in the short inlet, resulting in increased levels of incidence distortion and also contributing to the rotor performance degradation.

At the off-design conditions, the fan performance is reduced relative to the baseline case, since the short inlet does not mitigate the inflow non-uniformities as well as the long inlet. At the wing C_{Lmax} condition, the inflow non-uniformity is largest and consequently, the fan efficiency is reduced the most. The stagnation point streamlines and the absolute Mach number distributions are shown in the top left and center in Fig. 16 for the baseline and the *L/D* = 0.25 designs, respectively. The axial Mach number distributions in the inlet flow are depicted at the bottom in Fig. 16. The inlet flow accelerates around the inlet lip, resulting in a supersonic flow region followed by a shock. A thinner LE shape is required in the short-inlet design to limit the external flow acceleration at cruise. As a result, the over-speed along the inlet internal surface is increased at the wing

C_{Lmax} condition. By controlling the curvature change along the inlet internal shape, the shock strength is limited and a shock-induced inlet flow separation is avoided.

Similar to the cruise condition, the local region of high Mach number shifts towards the fan face in the short inlet. The spanwise distributions of the axial Mach number and the rotor incidence along the bottom inlet fan face are depicted in Fig. 17. Relative to the baseline propulsor, the maximum Mach number at the fan face increases by $\Delta M_{x,max}$ = 0.17 and the minimum incidence is reduced by up to Δi = -10° near the shroud. Locally, the rotor operates near choke, resulting in substantial fan efficiency penalties. To alleviate the incidence distortion, the rotor blades were re-cambered over the outer span. As a result, the minimum incidence was increased by up to Δi_{min} = +2°, leading to a fan efficiency benefit.

As listed in Table 2, the candidate short-inlet design with *L/D* = 0.19 enables a -17.8 % reduction in cruise nacelle drag relative to the baseline propulsor. However, as indicated in the right-hand plots in Fig. 15, the interaction of the rotor with the non-uniform inlet flow is further enhanced, resulting in a fan efficiency penalty of -1.63 %. The rotor performance reduction is large enough to outweigh the drag benefits and the propulsive efficiency is reduced by -0.80 % relative to the baseline. Similarly, the rotor performance decreases at off-design due to the increase in the incidence distortion. The Mach number distributions at the wing C_{Lmax} condition are depicted in the right-hand plots in Fig. 16 for the *L/D* = 0.19 design. The inlet flow is no longer fully attached and the maximum axial Mach number is further increased compared to the *L/D* = 0.25 design,
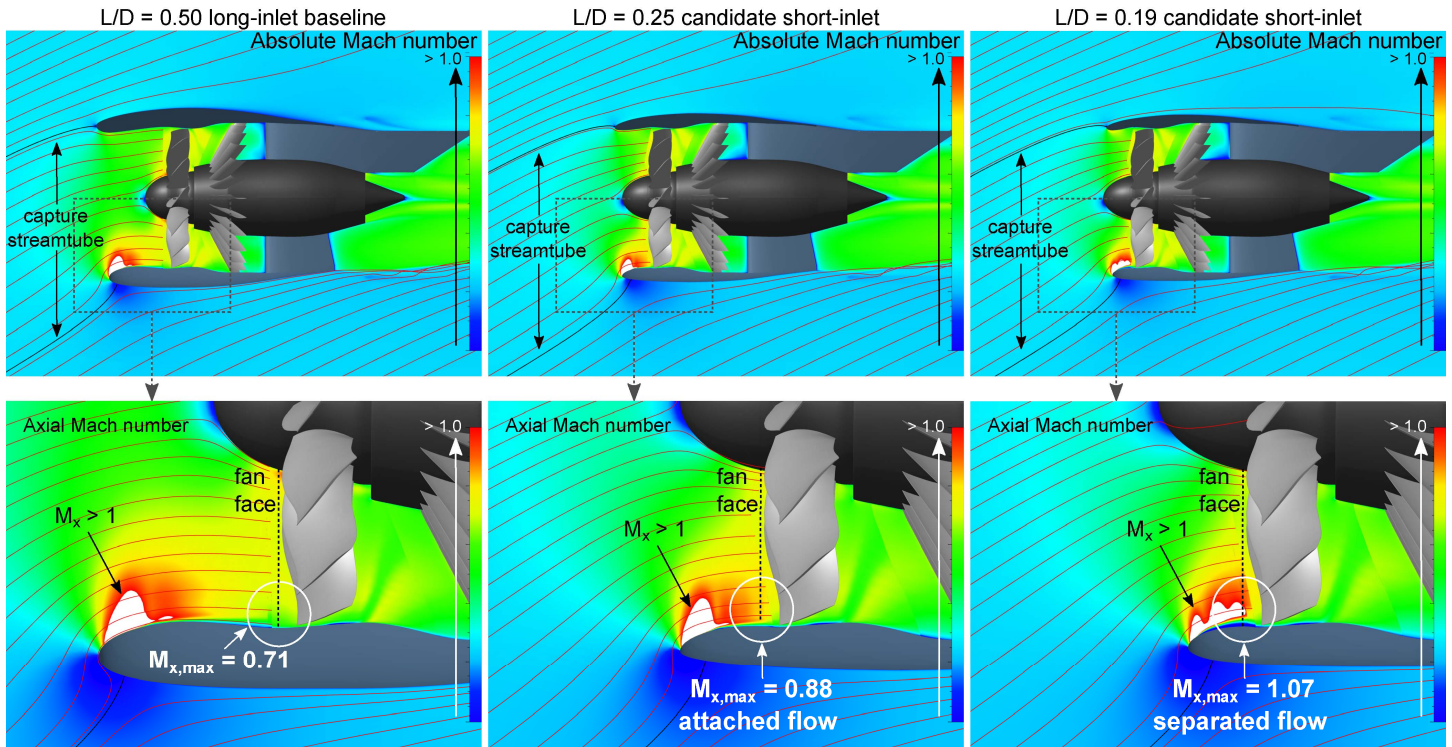
Fig. 16: Mach number distribution (top) and axial Mach number distribution (bottom) for the baseline propulsor (left) and the candidate short-inlet designs with *L/D* = 0.25 (center) and *L/D* = 0.19 (right) at the wing C_{Lmax} operating condition.
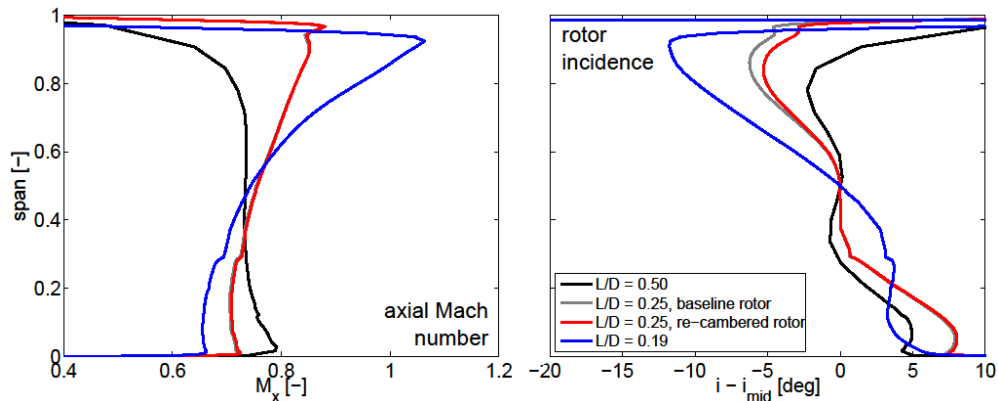

Fig. 17: Time-averaged spanwise profiles of axial Mach number (left) and rotor incidence relative to mid-span incidence (right) at the bottom fan face for the baseline (*L/D* = 0.5) and the candidate short-inlet propulsors (*L/D* = 0.25 and *L/D* = 0.19) at the wing C_{Lmax} condition.

leading to an additional reduction in rotor incidence, as shown on the right in Fig. 17. As a consequence, the fan efficiency penalty increases to -3.94 % relative to the long-inlet baseline.

The increased incidence distortion leads to a core inflow stagnation pressure distortion large enough to exhaust most of the LPC stability margin and possibly requiring modifications to the LPC such as variable-pitch inlet guide vanes (IGVs). For a feasible installation of a design with *L/D* = 0.19, advanced concepts are needed. The potential of two such concepts for improved rotor performance were determined. First, a blow-in door system in the inlet was demonstrated to eliminate flow separation at the cross-wind condition and raise the rotor efficiency to within 1.5 % of the performance achieved by the

baseline propulsor. Second, the fan case was pitched by 5° to align the rotor axis of rotation with the incoming flow at cruise and thereby reduce the rotor incidence distortion, leading to a fan efficiency benefit of 0.8% at cruise. Details on the performance assessment of the two candidate short-inlet designs and a discussion of the blow-in door and pitched fan case concepts are given in [14].

The *L/D* = 0.25 design maintains the cruise propulsive efficiency of the baseline case while providing for separation-free inlet flow at the wing C_{Lmax} condition and limiting off-design rotor performance penalties. On the aircraft system level, the reductions in nacelle weight and drag are suggested to lead to fuel burn benefits relative to an aircraft powered by the

13

long-inlet baseline propulsor. As the inlet length is shortened beyond $L/D = 0.25$, the impact of the degraded rotor performance outweighs the benefits from additional reductions in nacelle drag and the propulsor performance decreases.

The results for inlet pressure recovery π_{inlet}, nacelle drag D_{nac}, fan efficiency η_{fan}, and propulsive efficiency η_{prop} are plotted in Fig. 18 for the baseline and the two candidate short-inlet propulsors. All of the results are relative to the baseline propulsor. The data points are connected by trend lines. The dependence of the inlet pressure recovery and the nacelle drag on inlet length over fan diameter L/D is close to linear. However, the fan efficiency, which drives the changes in propulsive efficiency, is non-linear in inlet L/D. Guided by the sensitivity analysis, the trend in the propulsive efficiency is constructed from the curves for π_{inlet}, D_{nac}, and η_{fan}. The maximum in propulsive efficiency is suggested to fall between an L/D of 0.25 and 0.4.
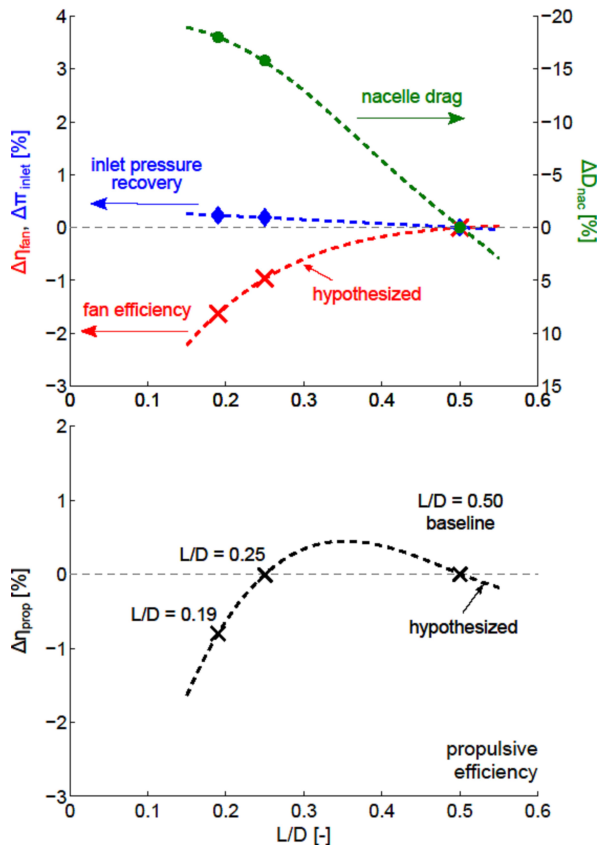

Fig. 18: Hypothesized trend in propulsive efficiency with inlet
L/D (bottom) as a result of the trade-offs between fan
efficiency, nacelle drag, and inlet pressure recovery (top).

SUMMARY AND CONCLUSIONS

Low-FPR propulsors offer the potential for significant fuel burn benefits over current turbofan designs but require short inlets and nacelles to minimize the impact of larger diameter fans on their weight and drag. An integrated design capability for short inlets and nacelles was developed by combining a spline-based tool to define inlet and nacelle surface geometries with a 3D body force method to represent the rotor and stator blade rows. The low computational cost enabled by the body force simulations allows the framework to be used for the parametric exploration of the short-inlet design territory and the optimization of candidate inlet and nacelle shapes.

The interaction of the fan rotor with a region of high Mach number over the outer span at the fan face and the reduced flow straightening through the inlet are identified as the critical aerodynamic mechanisms limiting the design of short inlets. Both mechanisms lead to an increase in incidence distortion and a reduction in the fan efficiency relative to long inlets.

A design strategy based on supercritical airfoils for the top nacelle profile and a parametric description for the bottom inlet shape enabled the design of a short inlet with $L/D = 0.25$ which maintains the isolated propulsor performance of the long-inlet baseline configuration with $L/D = 0.5$. The short-inlet propulsor offers a 16 % nacelle drag reduction at cruise and provides for separation-free inlet flow at off-design conditions. An L/D of 0.25 is suggested to represent the shortest possible inlet length for equal or better propulsive efficiency relative to a long-inlet propulsor with $L/D = 0.5$. For inlets with $L/D < 0.25$, the increase in the fan efficiency penalties outweigh the benefits from additional reductions in nacelle drag. The recommended inlet length for benefits in propulsor performance without jeopardizing operability is conjectured to be an L/D between 0.25 and 0.4.

Future work includes the assessment of a short-inlet configuration with an L/D between 0.3 and 0.4 in order to prove the hypothesis of improved propulsive efficiency relative to the baseline case and the performance assessment on the aircraft system level to quantify the potential fuel burn benefits due to reduced nacelle drag and weight. The design framework could be extended to include the engine-out "wind-mill" condition which can cause a substantial increase in wave drag due to flow spillage over the nacelle leading edge and should be accounted for in the design considerations. Finally, installation challenges due to the larger diameters of low-FPR, high-BPR propulsors and the reduction in fan noise attenuation potential and shield opportunities provided by short inlets should be addressed.

REFERENCES
[1] Green, J., 2005, "Mitigating the Environmental Impact of Aviation: Opportunities and Priorities," Report of the Greener by Design Science and Technology Sub-Group, the Royal Aeronautical Society.
[2] Owens, R., Hasel, K., and Mapes, D., 1990, "Ultra High Bypass Turbofan Technologies for the Twenty-First Century," AIAA 1990-2397.

[3] Suder, K., Delaat, J., Hughes, C., Arend, D., and Celestina, M., 2013, "NASA Environmentally Responsible Aviation Project's Propulsion Technology Phase I Overview and Highlights of Accomplishments," AIAA 2013-0414.

[4] Cumpsty, N., 2010, "Preparing for the Future: Reducing Gas Turbine Environmental Impact – IGTI Scholar Lecture," J. Turb, **132**.

[5] Neise, W., and Enghard, L., 2003, "Technology Approach to Aero Engine Noise Reduction," Aerosp. Sci. Techn., **7**, pp. 352-363.

[6] Hall, C., and Crichton, D., 2007, "Engine Design Studies for a Silent Aircraft," J. Turb., **129**, pp. 479-487.

[7] de la Rosa Blanco, E., Hall, C., and Crichton, D., 2007, "Challenges in the Silent Aircraft Engine Design," AIAA 2007-454.

[8] Maclsaac, B., and Langton, R., 2011, "Gas Turbine Propulsion Systems," AIAA Education Series, 1st edition.

[9] Lord, W., MacMartin, D., and Tillman, T., 2000, "Flow Control Opportunities in Gas Turbine Engines," AIAA 2000-2234.

[10] Michel, U, 2007, "The Geared Turbofan Technology – Opportunities, Challenges, and Readiness Status," 1st CEAS European Air and Space Conference, Berlin, Germany, September 10-13, 2007.

[11] Hughes, C., 2011, "Aircraft Engine Technology for Green Aviation to Reduce Fuel Burn," AIAA 2011-3531.

[12] Dunican, M., 1987, "Installation of Innovative turbofan Engines on Current Transport Airplanes," AIAA 1987-2921.

[13] Zimbrick, R., and Colehour, I., 1988, "An Investigation of Very High Bypass Ratio Engines for Subsonic Transports," AIAA 1988-2953.

[14] Peters, A., 2013, "Ultra-Short Nacelles for Low-FPR Propulsors," Ph.D. Thesis, Massachusetts Institute of Technology.

[15] Seddon, J., and Goldsmith, E., 1999, "Intake Aerodynamics," volume II of AIAA Education Series.

[16] Iek, C., Boldman, D., and Ibrahim, M., 1995, "Three-Dimensional Viscous Flow Analysis of an Advanced Ducted Propeller Subsonic Inlet, J. Prop. Power, **11**(2), pp. 236-243.

[17] Hsiao, E., Naimi, M., Lewis, J., Dalbey, K., Gong, Y., and Tan, C., 2001, "Actuator Duct Model of Turbomachinery Components for Powered-Nacelle Navier-Stokes Calculations," J. Prop. Power, **17**(4), pp. 919-927.

[18] Boldman, D., Iek, C., Hwang, D., Jeracki, R., Larkin, M., and Sorin, G., 1991, "Evaluation of Panel Code Predictions With Experimental Results of Inlet Performance for a 17-Inch Ducted Prop/Fan Simulator Operating at Mach 0.2," AIAA 1991-3354.

[19] Boldman, D., Iek, C., Hwang, D., Larkin, M., and Schweiger, P., "Effect of a Rotating Propeller on the Separation Angle of Attack and Distortion in Ducted Propeller Inlets," AIAA 1993-0017.

[20] Larkin, M., and Schweiger, P., 1992, "Ultra High Bypass Nacelle Aerodynamics: Inlet Flow-Through Nacelle High Angle of Attack Distortion Test," NASA CR-1992-189149.

[21] Mendenhall, M., and Spangler, S., 1970, "Theoretical Study of Ducted Fan Performance," NASA CR-1970-1495.

[22] Hirose, N., and Asai, K., 1991, "Euler Flow Analysis of Turbine Powered Simulation and Fanjet Engine," J. Jet Propulsion, **7**(6), pp. 1015-1022.

[23] Uenishi, K., Pearson, M., Lehnig, T., and Leon, R., "CFD-Based 3D Turbofan Nacelle Design System," AIAA 1990-3081.

[24] Chen, H, Yu, N., Rubber, P., and Jameson A., "Flow Simulations for General Nacelle Configurations Using Euler Equations," AIAA 1983-0539.

[25] Bush, R., 1997, "Engine Face and Screen Loss Models for CFD Applications," AIAA 1997-2076

[26] Unno, M., Kodama, H., Nozaki, O., and Nishizawa, T., 2001, "Unsteady Three Dimensional Navier-Stokes Simulations for Fan-OGV-Strut-Pylon Interaction," ISABE-2001-1197.

[27] Zimbrick, R., and Colehour, I., 1988, "An investigation of Very High Bypass Ratio Engines for Subsonic Transports, AIAA 1988-2953.

[28] Daggett, D., 2002, "Ultra-Efficient Engine Technology Systems Integration and Environmental Assessment," NASA CR-2002-211754.

[29] Daggett, D., Brown, S., and Kawai, R., 2003, "Ultra-Efficient Engine Diameter Study, NASA CR-2003-212309.

[30] Harris, C., 1990, "NASA Supercritical Airfoils," NASA TP-2969.

[31] Langley, M., 1979, "The Design of Axisymmetric Cowls for Podded Nacelles for High By-Pass Turbofan Engines," Aeronautical Research Council.

[32] Barber, T., Ives, D., Nelson, D., and Miller, R., 1985, "Computational Design and Validation Tests of Advanced-Concept Subsonic Inlets," J. Prop., **1**(2), pp. 97-102.

[33] Numeca FINE/Turbo 8.10-3, 2012, www.numeca.com

[34] Spalart, P., and Allmaras, S., 1992, "A One-Equation Turbulence Model for Aerodynamic Flows," AIAA 1992-0439.

[35] Marble, F., 1964, "Three-Dimensional Flow in Turbomachines," in High Speed Aerodynamics and Jet Propulsion, volume X, Hawthorne, W. R., pp. 83-166.

[36] Gong, Y., Tan, C., Gordon, K., and Greitzer, E., 1999, "A Computational Model for Short-Wavelength Stall Inception and Development in Multistage Compressors," J. Turb., **121**, pp. 726-734.

[37] Gong, Y., 1999, "A Computational Model for Rotating Stall and Inlet Distortions in Multistage Compressors," Ph.D. Thesis, Massachusetts Institute of Technology.

15